AIP | Journal of Applied Physics

Indium tin oxide-free transparent and conductive electrode based on SnOx | Ag | SnOx for organic solar cells

A. Bou, Ph. Torchio, D. Barakel, F. Thierry, A. Sangar, P.-Y. Thoulon, and M. Ricci

Citation: Journal of Applied Physics **116**, 023105 (2014); doi: 10.1063/1.4886225
View online: http://dx.doi.org/10.1063/1.4886225
View Table of Contents: http://scitation.aip.org/content/aip/journal/jap/116/2?ver=pdfcov
Published by the AIP Publishing

Indium tin oxide-free transparent and conductive electrode based on SnO_x | Ag | SnO_x for organic solar cells

A. Bou,[1,2] Ph. Torchio,[2,a)] D. Barakel,[2] F. Thierry,[2] A. Sangar,[3] P.-Y. Thoulon,[1] and M. Ricci[1]
[1]*CROSSLUX, Immeuble CCE, Avenue Georges Vacher, ZI Rousset Peynier, 13106 Rousset Cedex, France*
[2]*Institut Matériaux Microélectronique Nanosciences de Provence-IM2NP, Aix-Marseille Université, CNRS, UMR 7334, Domaine Universitaire de Saint-Jérôme, Service 231, 13397 Marseille Cedex 20, France*
[3]*Institut Matériaux Microélectronique Nanosciences de Provence-IM2NP, Université de Toulon, CNRS, UMR 7334, Bâtiment R, BP 132, 83957 La Garde Cedex, France*

(Received 17 April 2014; accepted 20 June 2014; published online 10 July 2014)

A SnO_x | Ag | SnO_x multilayer deposited by E-beam evaporation is proposed as transparent anode for a (poly-3-hexylthiophene):[6,6]-phenyl-C_{61}-butyric acid methyl ester (P3HT:PCBM) bulk heterojunction based Organic Solar Cell (OSC). Such multilayers are studied and manufactured with the objective to give to the electrode its best conductivity and transparency in the visible spectral range. A transfer matrix method numerical optimization of the thicknesses of each layer of the electrode is developed to limit the number of test samples which would have been manufactured whether an empirical method was chosen. Optical characterization of the deposited SnO_x and Ag thin films is performed to determine the dispersion of the complex refractive indices which are used as input parameters in the model. A satisfying agreement between numerical and experimental optical properties is found. The bare tri-layer electrodes show low sheet resistance (as low as 6.7 Ω/□) and the whole Glass | SnO_x | Ag | SnO_x structure presents a mean transparency on 400–700 nm spectral band as high as 67%. The multilayer is then numerically studied as anode for a P3HT:PCBM bulk heterojunction based OSC. Intrinsic absorption inside the sole active layer is calculated giving the possibility to perform optical optimization on the intrinsic absorption efficiency inside the active area by considering the media embedding the electrodes. An additional study using the morphology of the silver inserted between both oxide layers as input data is performed with a finite difference time domain 3D-method to improve the accordance between optical measurements and numerical results. © *2014 AIP Publishing LLC*.
[http://dx.doi.org/10.1063/1.4886225]

I. INTRODUCTION

The sun gives us a massive renewable source of energy that can be collected in several ways. One of them is to convert the photons of the solar spectrum into electricity via a photovoltaic (PV) device. The possibilities of materials and structures to achieve such devices are vast and until the last two decades were dominated by silicon and thin-film technologies. The production price and energetic cost of the crystalline silicon modules are currently high. Emerging PV devices as Organic Solar Cells (OSC) have the advantage of low manufacturing cost, high absorption coefficient, semi-transparency, and mechanical flexibility. OSCs are a very promising way for the next PV generation. Efficiency has moved up in the past years from a few percent to 12%.[1–4] Indium Tin Oxide (ITO) is one of the most used Transparent Conductive Oxides (TCOs) as OSC's transparent electrode. Unfortunately, indium is rare on earth and could become very expensive. Moreover, the sheet resistance (R_S) of ITO can significantly increase with cyclic bending beyond low bending radius (<10 mm).[5,6] Cracks can occur affecting the quality of the OSC. Investigating an alternative to ITO is a substantial research field.[7]

One solution is addressed by an Oxide | Metal | Oxide (OMO) multilayer structure[8–14] that can give a Transparent and Conductive Electrode (TCE) with sheet resistance under 10 Ω/□[12,15–18] and transparency as high as those of ITO in a defined spectral range.[19,20] A supplementary advantage is that OMO structure appears more resistant to cyclic bending[5,21] compared with ITO. The OMO electrode also limits the exposition of the bulk heterojunction active layer of the OSC to humidity thanks to the thin metal film.[22–24]

This paper presents an efficient way to optically optimize such OMO structures. The need of an optimization protocol results from the huge required time for realization of multiple OMO samples with disparate thicknesses and materials[10] and from the probable wasted time to test each possibility in an OSC. Indeed, the thicknesses of both oxide layers could vary from some nanometers to values sometimes above 50 nm. Furthermore, the optimum of transmittance is obtained when both oxide layers thicknesses are determined with a precision of less than 5 nm. The aim is then to quickly predict the optimized opto-geometrical parameters of such electrodes. The OMO structure integrates a very thin metal layer with thickness generally around 10 nm. Below 20 nm, a strong link exists between the optical constants and the thickness of the thin metal layer.[25,26] Additionally, the morphology observed by Scanning Electron Microscope (SEM) shows not fully metal-covered surface for thicknesses around

a)Author to whom correspondence should be addressed. Electronic mail: philippe.torchio@univ-amu.fr. Phone: +33 (0) 4 91 28 83 49. Fax: +33 (0) 4 91 28 88 52. URL: http://www.im2np.fr/perso/torchio.html.

10 nm.[12,27,28] The effective optical constants of silver should consider these geometrical particularities before to be entered in our model. Similarly, the optical constants of an oxide like SnO_2, ZnO, and others are sensitive to the thickness of the film for a sub-micrometric layer, and even drastically sensitive under 100 nm.[29–32] Another parameter to be considered is the probable diffusion of silver into both oxides[20,33] which can also impact the optical constants of oxide.

In this paper, the numerical optical optimization[34,35] of OMO structures based on a SnO_x | Ag | SnO_x electrode[17,27,36,37] is investigated by introducing in the model several parameters among those previously described. We also manufactured the SnO_x | Ag | SnO_x structures in a continuous vacuum atmosphere by E-beam evaporation.

II. SIMULATION AND EXPERIMENTAL DETAILS

A. Simulation details

An optical simulation through a Transfer Matrix Method (TMM)[11,27,35,38–40] is performed. This method allows us to calculate the amplitude of the electromagnetic wave at each interface of a multilayer and to obtain the reflectance R, the transmittance T, and the absorbance A of the stack. We have the possibility to calculate the absorption inside a single layer of the stack. This one-dimensional simulation method is rather fast to perform (less than one second for one calculation). A three-dimensional optical simulation is also performed by a Finite Difference Time Domain (FDTD) method[27,34,41,42] which rigorously solves Maxwell's equations and makes it possible to obtain the electromagnetic field versus time and position. The calculations were set up by using a resolution spatial grid of 1 nm for silver and 2 nm for oxides, during 1000 fs, with a time step of 1.9×10^{-3} fs. Appropriate boundary conditions were also used. This method requires more calculation time and memory space, due to the spatial and time meshing, but allows us to design three-dimensional structures.

The objectives of simulations are here to corroborate the optical R, T, and A measurements to the numerical results of single layers and multilayers and to obtain the optimal transmission in a defined spectral range by varying the thicknesses of both oxide layers with a given thickness of silver.

In the TMM, a simple one-dimensional design [Fig. 1(a)] with effective complex refractive indices of Ag and SnO_x layers [Fig. 3(a)] is used. With the FDTD method, we first replicate the one-dimensional design [Fig. 1(a)] to make sure that the correspondences between both models are right [Fig. 4]. In a second step, we will still use measured complex refractive index of SnO_x, and we will replace the effective complex refractive index of Ag by the bulk refractive index of Ag[43] while introducing its two-dimensional structure thanks to SEM images (Fig. 8). This structured Ag layer is sandwiched between two SnO_x layers as an attempt to obtain a more realistic three-dimensional design [Fig. 1(b)].

B. Experimental details

Samples were prepared on cleaned VWR® cut edges plain glass slides measuring $76 \times 26\,mm^2$ with a thickness of 1 mm. Substrates are presented into an Oerlikon Leybold Vacuum Univex 300 E-beam evaporator at normal incidence and with a distance of 20 cm from the liner containing the material to be deposited. The Ag thin film was deposited—from 99.99% pure Ag into a 4 cc Al_2O_3 liner—at an average rate of 1.5 nm s^{-1} and a pressure around 2×10^{-5} mbar. The SnO_x layer was deposited—from 99.995% pure SnO_2 into a 4 cc Mo liner—at an average rate of 0.2 nm s^{-1} and a pressure around 1×10^{-4} mbar. The thickness is calibrated from a quartz crystal oscillator monitor placed near the substrate during the deposition then checked by a mechanical profilometer.

Samples are optically characterized by spectrophotometry, including an integrating sphere. The absorption spectra (A = 1-R-T) are deduced from measurements of R and T. A Carl Zeiss ULTRA® VP 40 SEM was used to obtain images of silver morphology on glass (Fig. 8). The optical indices

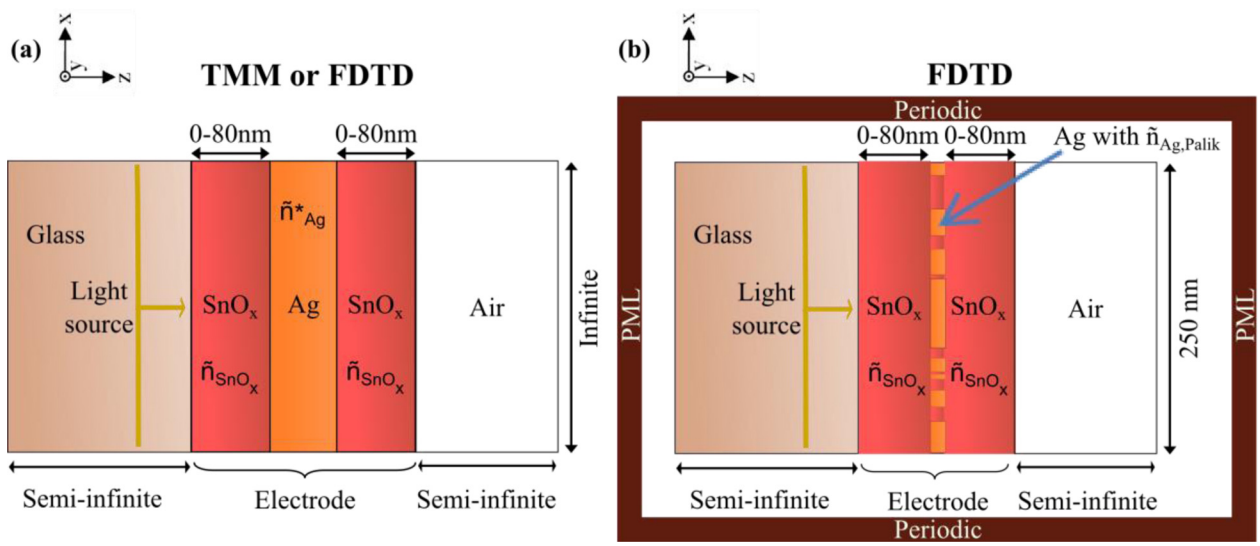

FIG. 1. (a) One-dimensional design calculated by TMM or FDTD model. (b) Three-dimensional design calculated by FDTD model.

are deduced from measurements done with a GES5E SEMILAB Spectroscopic Ellipsometer.

Electrical measurements of a sole Ag layer on glass, an SnO_x | Ag bilayer, and an SnO_x | Ag | SnO_x trilayer are performed with a CPS Resistivity Test Fixture from CASCADE® combined with a C4S 4-Point Probe Head.

III. RESULTS AND DISCUSSION

A. Numerical modeling with one-dimensional design and experimental results of the bare SnO_x | Ag | SnO_x electrode

The following structures: Glass | Ag, Glass | SnO_x | Ag, and Glass | SnO_x | Ag | SnO_x were first manufactured and optically characterized by spectrophotometry. The thicknesses and deposition rates of Ag were varied. For low deposition rates ($\sim$1 Å s^{-1}), we observed a peak of absorptance from the Glass | Ag structure that can reach 40% for wavelengths around a midpoint value which could vary from 500 nm to 550 nm when the Ag thickness grows from 8 to 10 nm (Fig. 2). This could stem from of an island-like morphology presenting a Surface Plasmon Resonance (SPR) which is known to enhance absorption.[44] The absorptance peak depends on the shape and the size of the nanoparticles,[45] themselves possibly modified by the increase in the deposited metal thickness. The sheet resistance was also measured at low deposition rates ($\sim$1 Å s^{-1}); the R_S values were higher than 1 kΩ/□ for metal thicknesses close to 10 nm and around 200 Ω/□ for a 15 nm-thick Ag layer. The surface reactivity of the Ag-islands[46] could induce this low conductivity like the isolated island-like morphology, since no electrical connections exist between the different parts of the surface sample. From these results, we decided to gradually increase the Ag deposition rate from 1 to 15 Å s^{-1} implying a decrease in R_S for the same Ag thickness. A similar electrical behavior of sheet resistance versus silver thickness for several Ag deposition rates was noticed for Glass | SnO_x | Ag (Fig. 2) and Glass | SnO_x | Ag | SnO_x structures. The R_S values of these samples were slightly higher when Ag is deposited on SnO_x substrate instead of glass (i.e., from 3 Ω/□ on glass to 10 Ω/□ on SnO_x for a 10 nm-thick Ag layer deposited at 1.5 nm s^{-1} deposition rate). This could be due to the diffusion of Ag inside the oxide and/or to the higher roughness of SnO_x compared with glass impinging on the morphology of Ag.

From these observations, we fix the deposition rate at 1.5 nm s^{-1}. The Ag thickness is maintained at 10 nm, because as we determined it in this study and as proved experimentally in others studies,[36,47] it is found to be the best compromise between high conductivity and high transparency for such trilayers.

Spectroscopic ellipsometer measurements were performed on 30 nm-thick SnO_x single layer and 10 nm-thick Ag single layer deposited on glass to obtain the $\tilde{n}_{30nm\text{-}SnOx}$ and $\tilde{n}_{10nm\text{-}SnOx}$ optical constants, respectively, presented in Figure 3(a). These optical constants are deduced from the fit of tan(Ψ) and cos(Δ) measurements over five different angles of incidence/reflection from 55° to 75°. Figure 3(b) shows a good agreement between measured and calculated—with TMM model—values of R, T, and A for the Glass | SnO_x (30 nm) structure. By integrating these optical constant values in the models, we are able to calculate R, T, and A for other designs, such as Glass | SnO_x (45 nm) | Ag (10 nm) | SnO_x (45 nm). Both numerical TMM and FDTD models for 1D-design (Fig. 4) were employed to obtain these optical properties giving comparable results. The slight differences can be explained mainly by the way indices are taken into account in the models. In TMM model, indices are interpolated from ellipsometric experimental data while indices are fitted with a polynomial law in FDTD model.

Calculated R, T, and A versus wavelength for Glass | SnO_x (t_1 nm) | Ag (10 nm) | SnO_x (t_2 nm) structures using the 1D-design TMM method are compared with experimental measurements in Figure 5 for some selected oxide thicknesses, $t_1 = t_2 = 19$, 32, 45, and 59 nm. The numerical values are corrected to take into account the first reflectance of light on the glass from outside, because the models integrate the light source in the glass as shown in Figure 1. A satisfying accordance is observed for different SnO_x thicknesses in the electrodes between simulated and measured optical properties curves.

To quantify the differences between numerical (α) and experimental (β) curves, we used the mean absolute percentage error (MAPE). For transmittance, the MAPE is equal to

$$\mathrm{MAPE} = \frac{1}{n}\sum_{i=1}^{n}\left|\frac{T_{i,\alpha} - T_{i,\beta}}{T_{i,\alpha}}\right|, \quad (1)$$

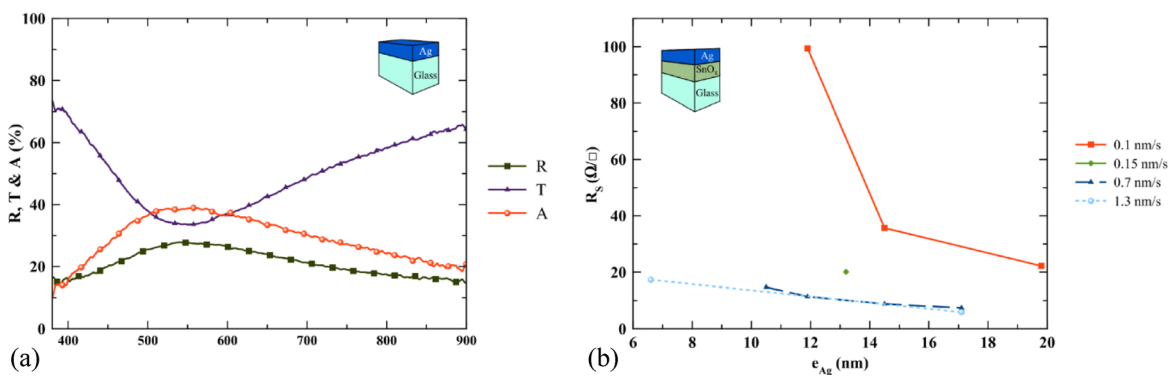

FIG. 2. Left: measured transmittance T, reflectance R, and absorptance A of a 9 nm-thick Ag layer deposited on glass at around 0.2 nm/s; right: sheet resistance R_S versus thickness of Ag layers e_{Ag} deposited on a 30 nm-thick SnO_x with several deposition rates (0.1, 0.15, 0.7, and 1.3 nm/s).

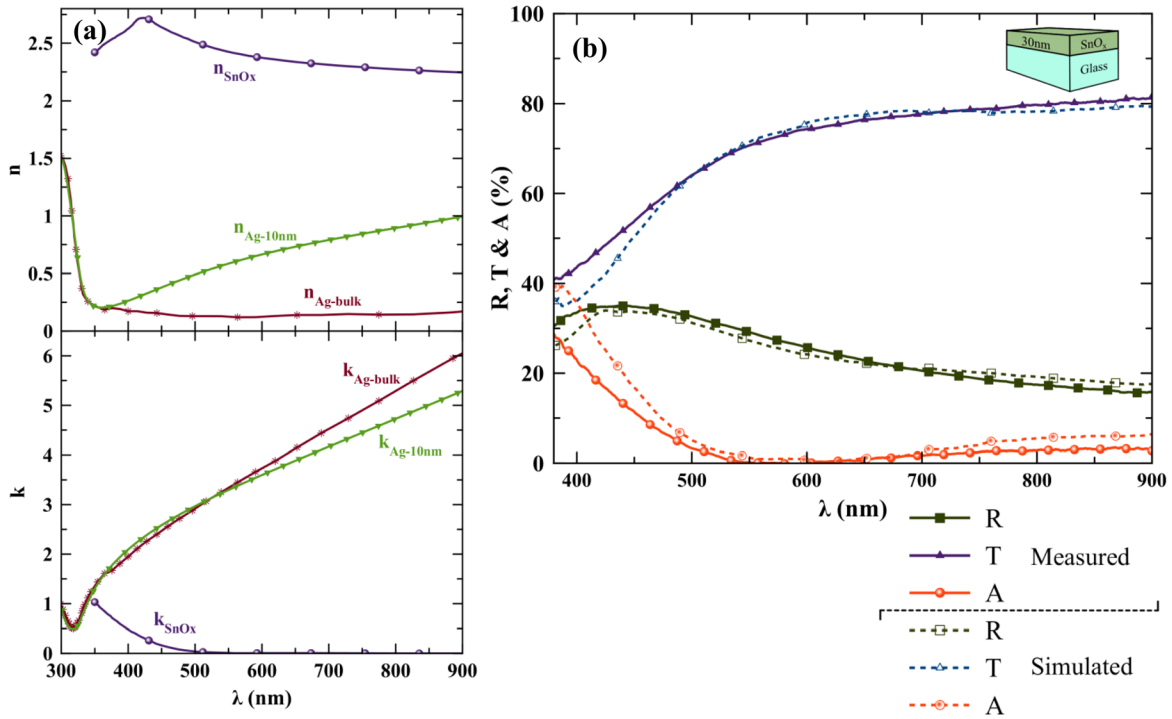

FIG. 3. (a) Top: Bulk refractive index n of Ag[43], measured n of 30 nm-thick SnO_x and measured n of 10 nm-thick Ag; Down: bulk extinction coefficient k of Ag[43], measured k of 30 nm-thick SnO_x and measured k of 10 nm-thick Ag. (b) Experimental and numerical (1D-TMM) transmittance T, reflectance R, and absorptance A of Glass | SnO_x (30 nm) integrating for simulation the complex refractive index of 30 nm-thick SnO_x.

where i is the i-th wavelength and n is the total number of wavelength points (the same formula could be used for A and R by replacing T). The MAPE values—α being TMM result and β measurement in Eq. (1)—averaged over the four measured electrodes presented in Figure 5 are for R, T, and A, respectively, 24.7%, 7.5% and 16.3%. We obtain a low discordance value for T which is our data of interest.

The arithmetic mean transmittance T_{mean} on a given spectral range is also generally defined and can be obtained by

$$T_{mean} = \frac{\int_{400\,nm}^{700\,nm} T(\lambda) d\lambda}{\int_{400\,nm}^{700\,nm} d\lambda}. \quad (2)$$

The arithmetic mean transmittance for wavelengths ranging between 400 and 700 nm about the Glass | SnO_x (44 nm) | Ag (10 nm) | SnO_x (40 nm) structure (Fig. 6) is then 65.3%. The optical T_{mean} and electrical R_S values of several electrodes comprising those presented in Figure 5 can be found in Table I. This table also provides the transmittance T_{550} at the wavelength of 550 nm and the figures of merit Φ_{T550} and Φ_{Tmean} of the manufactured electrodes. The figure of merit, proposed by Haake,[48] for transparent conductors is given by

$$\phi_T = \frac{T^{10}}{R_s}. \quad (3)$$

The cartography of the mean transmittance T_{ms} convoluted by the AM 1.5 solar spectrum is presented in Figure 6 in order to deduce the optimal thicknesses set of SnO_x layers of the Glass | SnO_x (t_1 nm) | Ag (10 nm) | SnO_x (t_2 nm) electrode in air. The T_{ms} values are calculated from

$$T_{ms} = \frac{\int_{400\,nm}^{700\,nm} I_{AM1.5}(\lambda)\, T(\lambda)\, d\lambda}{\int_{400\,nm}^{700\,nm} I_{AM1.5}(\lambda)\, d\lambda}. \quad (4)$$

Both oxide layers' thicknesses are optimized by calculating T_{ms} in the considered 400–700 nm spectral band. We chose a variation step of 2 nm for t_1 and t_2 oxide thicknesses, ranging in the 0–80 nm scale. The optimum structure in air is demonstrated to be Glass | SnO_x (44 nm) | Ag (10 nm) | SnO_x (40 nm), giving a 71.6% T_{ms} value.

The sheet resistance measured between 6 and 18 Ω/□ is in the typical range of other similar efficient electrodes.[17,36] The relatively low transparency of SnO_x single layer for wavelengths below 500 nm [Fig. 3(b)] leads to low transparency in this frequency domain for the trilayer too (Fig. 5).

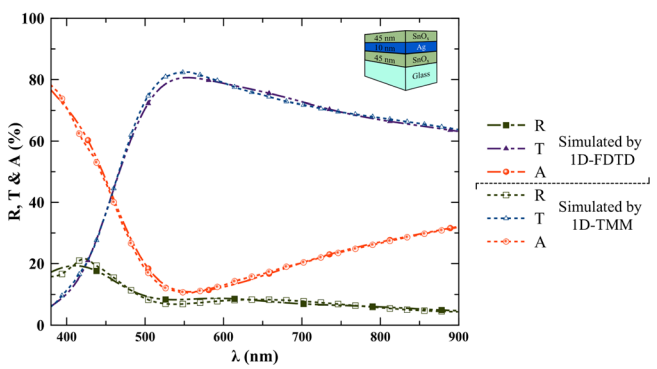

FIG. 4. Calculated transmittance T, reflectance R, and absorptance A obtained by both 1D-FDTD and 1D-TMM methods for structure: glass | SnO_x (45 nm) | Ag (10 nm) | SnO_x (45 nm).

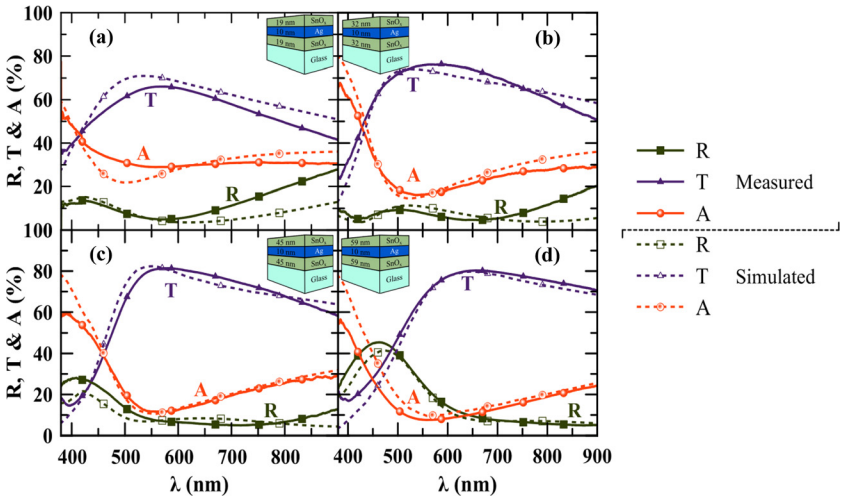

FIG. 5. Experimental and numerical (1D-TMM) transmittance T, reflectance R, and absorptance A of (a) glass | SnO_x (19 nm) | Ag (10 nm) | SnO_x (19 nm), (b) glass | SnO_x (32 nm) | Ag (10 nm) | SnO_x (32 nm), (c) glass | SnO_x (45 nm) | Ag (10 nm) | SnO_x (45 nm), and (d) glass | SnO_x (59 nm) | Ag (10 nm) | SnO_x (59 nm). A satisfying accordance is observed for different SnOx thicknesses in the electrodes between simulated and measured optical properties curves.

This is supposed to be due to a non-stoichiometric SnO_2, clarifying the SnO_x term used in this paper. We could improve of our deposition method of SnO_2 by using a flow of oxygen, hoping for a better mean transmittance. Finally, the significant agreement between simulation and measurement is a worthy result for this kind of structure and allows us to obtain experimental optima close to that calculated. The strength of our simulation models is to be also applicable to other materials.

B. Numerical results of the SnO_x | Ag | SnO_x electrode used as anode inside an OSC

Simulation can be applied to a whole OSC. A main objective for PV-scientists is to limit the manufacturing time by avoiding many production tests to find the optimal structure. For that, the intrinsic absorption efficiency in the active layer needs to be calculated from

$$\eta_{A_{\text{active layer}}} = \frac{\int_{\lambda_1}^{\lambda_2} A_{\text{active layer}}(\lambda) I_{AM1.5}(\lambda)\, d\lambda}{\int_{\lambda_1}^{\lambda_2} I_{AM1.5}(\lambda)\, d\lambda}. \quad (5)$$

Thus, a typical OSC presenting the following design: Glass | SnO_x (t_1 nm) | Ag (10 nm) | SnO_x (t_2 nm) | PEDOT:PSS (50 nm) | (poly-3-hexylthiophene):[6,6]-phenyl-C_{61}-butyric acid methyl ester (P3HT:PCBM) (180 nm) | Ag (100 nm) [Fig. 7(a)] can be optimized to get the best $\eta_{A_{\text{active layer}}}$ by varying the thicknesses of both SnO_x layers in the 0–80 nm scale [Fig. 7(b)]. We can then select the thicknesses which give the highest intrinsic absorption efficiency inside the active layer, i.e., P3HT:PCBM. We obtain thinner optimal thicknesses for both oxides than in the optimization of the bare electrode in air—$t_1 \approx 10$ nm and $t_2 \approx 15$ nm. In this thickness domain—below 15 nm—we cannot be sure that the model is still accurate. As can be seen in Figure 5(a), the measured transmission is around 5–10% below the simulated one. This could be the result of an optical constant change for very thin manufactured SnO_x layer. Furthermore, Ag diffusion in both oxide layers[20,33] during process could induce a change in optical constants on several nanometers close to the Ag layer. That means that the thinner the SnO_x layer, the higher the impact of the SnO_x optical constants modification on the numerical optical results due to Ag migration. Differences between real and simulated structures could result in a thickness shift of the optimum thicknesses for both SnO_x layers. In Figure 5, we can observe a slight red-shift of the wavelength for maximum T when the SnO_x thicknesses increase. This red-shift could also be linked to the variability of the SnO_x optical constants for SnO_x thicknesses under 50 nm correlated to the Ag diffusion in both oxides.

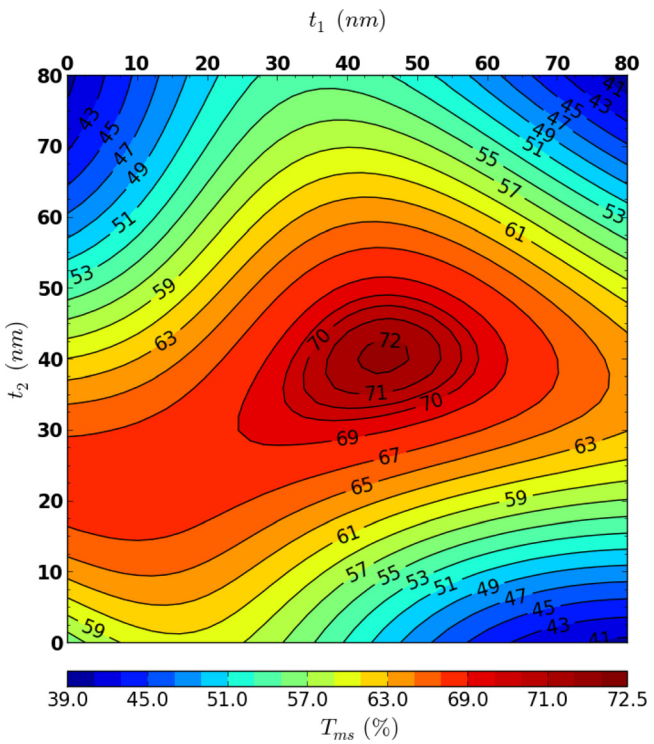

FIG. 6. Glass | SnO_x (t_1 nm) | Ag (10 nm) | SnO_x (t_2 nm) electrodes T_{ms} values for wavelengths ranging between 400 and 700 nm

C. Three-dimensional design integrating the Ag morphology applied to bare SnO_x | Ag | SnO_x electrode

The first consideration was to investigate the Ag structure at the surface of a glass substrate. Figure 8 presents SEM images of the silver percolation for 9 nm- and 10 nm-thick layers. The surfaces are not completely covered by silver and

TABLE I. Layer's thicknesses of SnO_x | Ag | SnO_x electrodes with their transmittance at 550 nm, their arithmetic mean transmittance between 400 and 700 nm, their sheet resistance and their factor of merit for both transmittance values.

			Transmittance (%)			Factor of merit ($m\Omega^{-1}$)	
Thickness of the glass side SnO_x (nm)	Thickness of Ag (nm)	Thickness of the air side SnO_x (nm)	At 550 nm	Averaged between 400 and 700 nm	Sheet resistance ($\Omega/\square$)	With the transmittance at 550 nm	With the arithmetic mean transmittance between 400 and 700 nm
19	10	19	65.8	59.5	16.1	0.95	0.34
19	10	59	58.6	53.9	17.5	0.27	0.12
30	10	30	73.5	63.6	15.3	3.00	0.71
32	10	32	75.8	65.4	14.5	4.32	0.99
40	10	53	75.6	65.8	16.4	3.72	0.93
45	10	45	80.7	64.0	10.7	10.9	1.08
47	10	45	78.5	61.7	6.7	13.3	1.19
53	10	40	80.4	66.9	18.0	6.27	1.00
59	10	59	67.2	58.1	17.3	1.09	0.25

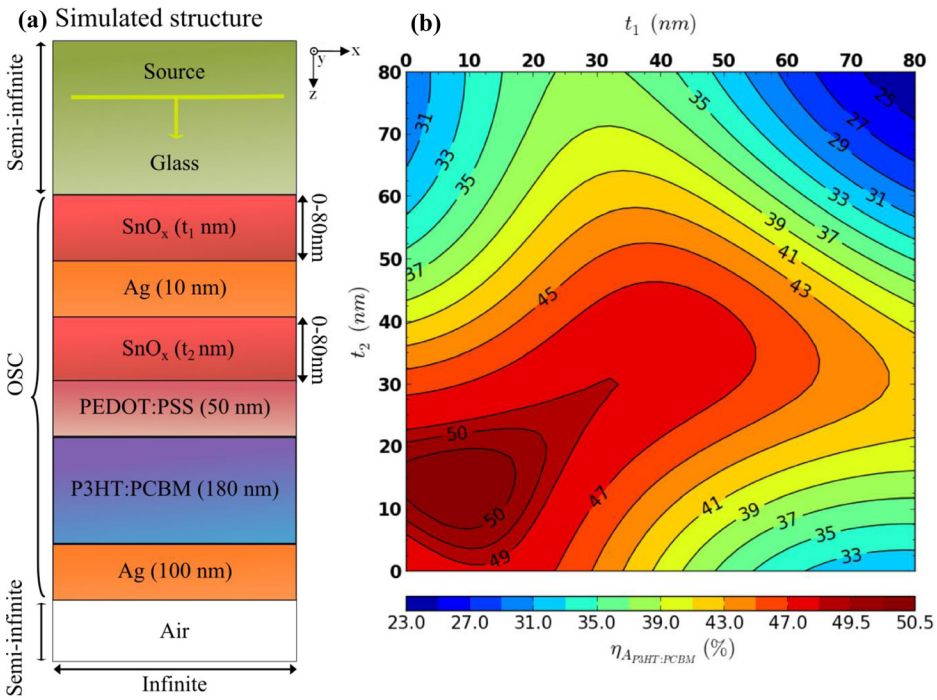

FIG. 7. (a) Design of the OSC with the trilayer as anode. (b) Intrinsic absorption efficiency inside P3HT:PCBM for wavelengths between 350 and 660 nm for the glass | SnO_x (t_1 nm) | Ag (10 nm) | SnO_x (t_2 nm) | PEDOT:PSS (50 nm) | P3HT:PCBM (180 nm) | Ag (100 nm) structure when varying the thicknesses t_1 and t_2 of both SnO_x layers.

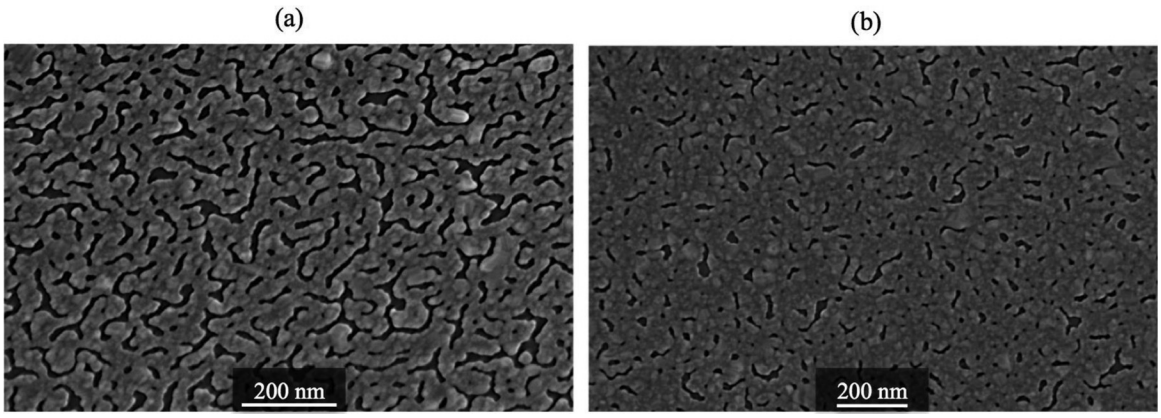

FIG. 8. SEM images showing the morphology of (a) 9 nm-thick Ag layer on glass and (b) 10 nm-thick Ag layer on glass.

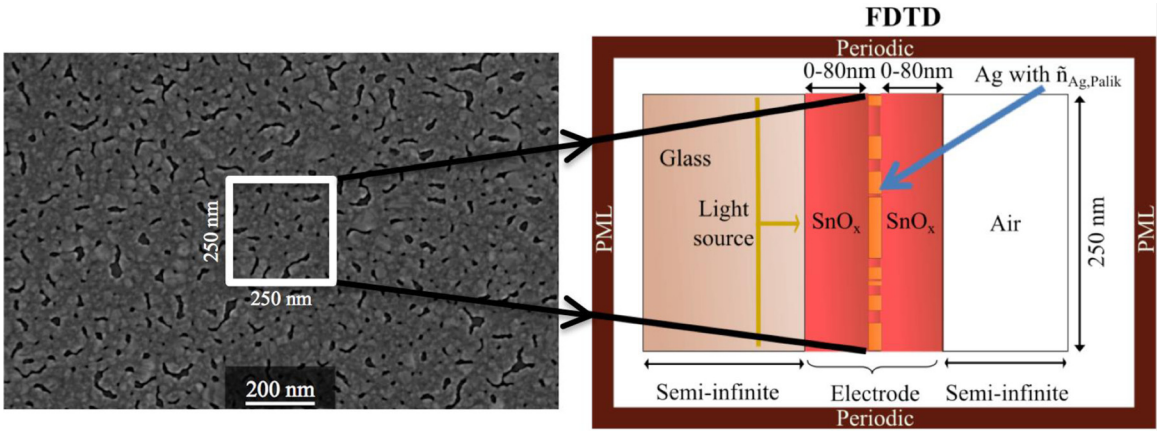

FIG. 9. A 250 nm^2 surface from SEM image (left) inserted in a 3D-FDTD model (right).

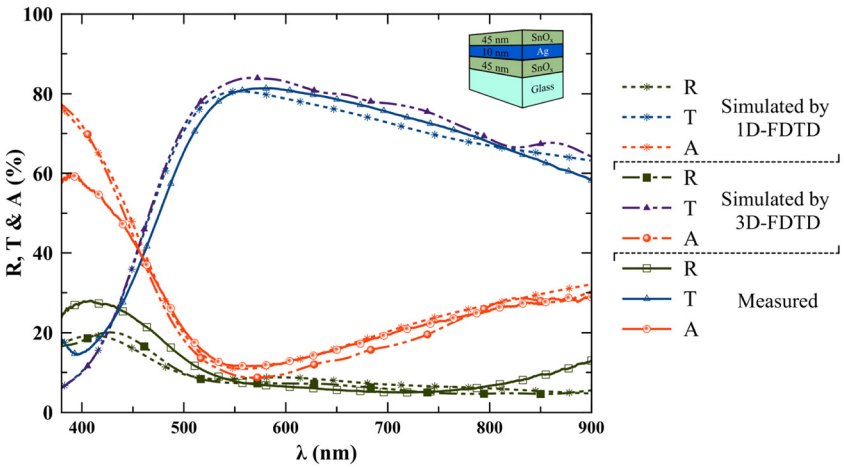

FIG. 10. Transmittance T, reflectance R, and absorptance A of glass | SnO_x (45 nm) | Ag (10 nm) | SnO_x (45 nm) calculated from the 3D-design for FDTD model, the 1D-design for FDTD model, and the experimental measurements.

reveal no isolated clusters as supposed by the electrical measurements. This morphology permits a high conductivity of the Ag layer without decreasing its transparency. It also limits the SPR phenomenon which could increase optical absorption[41,42,49–51] if the clusters are isolated (nanoparticles). Figure 8(a) shows a lower filling rate than Figure 8(b). Such morphology can be introduced in our FDTD model for simulation. By using the bulk complex refractive index of silver,[43] a 3D-design in air can be simulated by FDTD in order to compare results with experimental measurements and with the one-dimensional FDTD model [Fig. 4]. Figure 10 shows the measured and calculated optical results for the design presenting the best T_{550} in Table I (i.e., Glass | SnO_x (45 nm) | Ag (10 nm) | SnO_x (45 nm)). The 3D-FDTD calculation relies on a three-dimensional design (Fig. 9) for Ag which integrates a simulation zone for Ag of 250 nm^2 extracted from the center of Figure 8(b). A better agreement is confirmed between the 3D calculations and the experimental measurements than with the 1D-FDTD simulation. It is therefore demonstrated that SEM images of Ag structures can be used as input data to efficiently simulate trilayer electrodes.

IV. CONCLUSION

A numerical optimization method of oxide | metal | oxide trilayer transparent and conductive electrodes for OSC is presented in this paper. An agreement is demonstrated between manufactured and simulated electrodes for one-dimensional design introducing the dispersion couple ($\tilde{n}_{30nm\text{-}SnOx}(\lambda)$, $\tilde{n}_{10nm\text{-}Ag}(\lambda)$) of optical constants for 30 nm-thick SnO_x and 10 nm-thick Ag, respectively. Experimental Glass | SnO_x | Ag | SnO_x electrodes show sheet resistance as low as 6.7 Ω/□ and T_{mean} (for wavelengths ranging between 400 and 700 nm) as high as 67% taking in account R and A of the bare glass. Moreover, transparency increases up to a value of 80% at the wavelength of 550 nm. Such results are at the state of the art for such electrodes. However our optimization protocol could be applied to other kind of materials or application.

The numerical optimization of a multilayer electrode as anode inside an OSC was also performed and could be corroborated with experimental results in the future. In particular, we predict very low optimal thicknesses (around 15 nm) for both SnO_x layers. By introducing several optical constants depending on the depth in the SnO_x thickness and by taking into account the Ag diffusion (by adding for instance intermediate layers between SnO_x and Ag layers), our model could be further improved increasing the accuracy on the investigation of the optimal thicknesses.

A 3D-design integrating the real morphology of silver has been proved to describe efficiently the optical properties of real SnO_x | Ag | SnO_x structures. Further work needs to be done with this 3D-design concept to improve the quality of

the numerical transfer of SEM images (including Ag morphology observed upon SnO_x layer) or AFM mapping and to better approach the experimental measurements.

ACKNOWLEDGMENTS

The work presented in this paper was partially supported by the French Foundation of Technological Research (ANRT) under Grant No. CIFRE-2012/0731.

[1]R. F. Service, Science **332**, 293 (2011).
[2]M. A. Green, K. Emery, Y. Hishikawa, W. Warta, and E. D. Dunlop, Prog. Photovoltaics Res. Appl. **22**, 1 (2014).
[3]See http://www.nrel.gov/ncpv/ for the research-cell efficiency records chart (2014).
[4]*Heliatek Consolidates its Technology Leadership by Establishing a New World Record for Organic Solar Technology With a Cell Efficiency of 12%* (2013); http://www.heliatek.com/newscenter/latest_news/neuer-weltrekord-fur-organische-solarzellen-heliatek-behauptet-sich-mit-12-zell effizienz-als-technologiefuhrer/?lang=en.
[5]H. Cho, C. Yun, J.-W. Park, and S. Yoo, Org. Electron. **10**, 1163 (2009).
[6]K. Lim, S. Jung, J.-K. Kim, J.-W. Kang, J.-H. Kim, S.-H. Choa, and D.-G. Kim, Sol. Energy Mater. Sol. Cells **115**, 71 (2013).
[7]C. G. Granqvist, Sol. Energy Mater. Sol. Cells **91**, 1529 (2007).
[8]L. Cattin, Y. Lare, M. Makha, M. Fleury, F. Chandezon, T. Abachi, M. Morsli, K. Napo, M. Addou, and J. C. Bernède, Sol. Energy Mater. Sol. Cells **117**, 103 (2013).
[9]L. Cattin, M. Morsli, F. Dahou, S. Y. Abe, A. Khelil, and J. C. Bernède, Thin Solid Films **518**, 4560 (2010).
[10]C. Guillén and J. Herrero, Thin Solid Films **520**, 1 (2011).
[11]S. M. Durrani, E. Khawaja, A. Al-Shukri, and M. Al-Kuhaili, Energy Build. **36**, 891 (2004).
[12]J. C. Bernède, L. Cattin, T. Abachi, Y. Lare, M. Morsli, and M. Makha, Mater. Lett. **112**, 187 (2013).
[13]D.-T. Nguyen, S. Vedraine, L. Cattin, P. Torchio, M. Morsli, F. Flory, and J. C. Bernède, J. Appl. Phys. **112**, 063505 (2012).
[14]A. El Hajj, B. Lucas, M. Chakaroun, R. Antony, B. Ratier, and M. Aldissi, Thin Solid Films **520**, 4666 (2012).
[15]J.-A. Jeong and H.-K. Kim, Sol. Energy Mater. Sol. Cells **93**, 1801 (2009).
[16]D. R. Sahu and J.-L. Huang, Thin Solid Films **516**, 208 (2007).
[17]S. H. Yu, C. H. Jia, H. W. Zheng, L. H. Ding, and W. F. Zhang, Mater. Lett. **85**, 68 (2012).
[18]A. El Hajj, T. M. Kraft, B. Lucas, M. Schirr-Bonnans, B. Ratier, and P. Torchio, J. Appl. Phys. **115**, 033103 (2014).
[19]T. Abachi, L. Cattin, G. Louarn, Y. Lare, A. Bou, M. Makha, P. Torchio, M. Fleury, M. Morsli, M. Addou, and J. C. Bernède, Thin Solid Films **545**, 438 (2013).
[20]T. Winkler, H. Schmidt, H. Flügge, F. Nikolayzik, I. Baumann, S. Schmale, T. Weimann, P. Hinze, H. H. Johannes, T. Rabe, S. Hamwi, T. Riedl, and W. Kowalsky, Org. Electron. Phys. Mater. Appl. **12**, 1612 (2011).
[21]W. Cao, Y. Zheng, Z. Li, E. Wrzesniewski, W. T. Hammond, and J. Xue, Org. Electron. **13**, 2221 (2012).
[22]B. Henry, A. Erlat, A. McGuigan, C. R. Grovenor, G. A. Briggs, Y. Tsukahara, T. Miyamoto, N. Noguchi, and T. Niijima, Thin Solid Films **382**, 194 (2001).
[23]J.-A. Jeong, H.-K. Kim, and M.-S. Yi, Appl. Phys. Lett. **93**, 033301 (2008).
[24]S. Park, K. Jung, C. Yun, H. Cho, B.-S. Bae, and S. Yoo, J. Soc. Inf. Disp. **19**, 597 (2011).
[25]P. Zhao, W. Su, R. Wang, X. Xu, and F. Zhang, Phys. E **41**, 387 (2009).
[26]A. I. Maaroof and G. B. Smith, Thin Solid Films **485**, 198 (2005).
[27]A. Bou, P. Torchio, D. Barakel, F. Thierry, P.-Y. Thoulon, and M. Ricci, Proc. SPIE 8987, in Oxide-Based Mater Devices V (SPIE, San Francisco, CA, 2014), p. 898706.
[28]W.-S. Liu, Y.-H. Liu, W.-K. Chen, and K.-P. Hsueh, J. Alloys Compd. **564**, 105 (2013).
[29]K. Żukowska and E. Idczak, Thin Solid Films **85**, 327 (1981).
[30]R. Alvarez, J. C. González, J. P. Espinós, A. R. González-Elipe, A. Cueva, and F. Villuendas, Appl. Surf. Sci. **268**, 507 (2013).
[31]A. Karpinski, A. Ferrec, M. Richard-Plouet, L. Cattin, M. A. Djouadi, L. Brohan, and P.-Y. Jouan, Thin Solid Films **520**, 3609 (2012).
[32]A. Karpinski, N. Ouldhamadouche, A. Ferrec, L. Cattin, M. Richard-Plouet, L. Brohan, M. A. Djouadi, and P.-Y. Jouan, Thin Solid Films **519**, 5767 (2011).
[33]N. S. McIntyre, D. Johnston, W. J. Chauvin, W. M. Lau, K. Nietering, D. Schuetzle, K. Shankar, and J. E. Macdonald, Nucl. Instrum. Methods Phys. Res., Sect. B **12**, 389 (1985).
[34]S. Vedraine, A. El Hajj, P. Torchio, and B. Lucas, Org. Electron. **14**, 1122 (2013).
[35]A. Bou, P. Torchio, S. Vedraine, D. Barakel, B. Lucas, J.-C. Bernède, P.-Y. Thoulon, and M. Ricci, Sol. Energy Mater. Sol. Cells **125**, 310 (2014).
[36]J.-D. Yang, S.-H. Cho, T.-W. Hong, D. I. Son, D.-H. Park, K.-H. Yoo, and W.-K. Choi, Thin Solid Films **520**, 6215 (2012).
[37]S. J. Kim, E. A. Stach, and C. A. Handwerker, Thin Solid Films **520**, 6189 (2012).
[38]W. Yu, L. Shen, F. Meng, Y. Long, S. Ruan, and W. Chen, Sol. Energy Mater. Sol. Cells **100**, 226 (2012).
[39]S. A. Dyakov, V. A. Tolmachev, E. V. Astrova, S. G. Tikhodeev, V. Y. Timoshenko, and T. S. Perova, in *International Conference on Micro-Nano-Electronics 2009*, edited by K. A. Valiev and A. A. Orlikovsky (SPIE, Zvenigorod, Russian Federation, 2009), p. 75210G.
[40]F. Monestier, A. K. Pandey, J.-J. Simon, P. Torchio, L. Escoubas, and J.-M. Nunzi, J. Appl. Phys. **102**, 034512 (2007).
[41]S. Vedraine, P. Torchio, D. Duché, F. Flory, J.-J. Simon, J. Le Rouzo, and L. Escoubas, Sol. Energy Mater. Sol. Cells **95**, S57 (2011).
[42]S. Vedraine, P. Torchio, A. Merlen, J. Bagierek, F. Flory, A. Sangar, and L. Escoubas, Sol. Energy Mater. Sol. Cells **102**, 31 (2012).
[43]E. Palik, *Handbook of Optical Constants of Solids* (Elsevier, 1997).
[44]C. F. Bohren and D. R. Huffman, *Absorption and Scattering of Light by Small Particles* (Wiley, New-York, 1983).
[45]N. Grillet, D. Manchon, F. Bertorelle, C. Bonnet, M. Broyer, E. Cottancin, J. Lermé, M. Hillenkamp, and M. Pellarin, ACS Nano **5**, 9450 (2011).
[46]N. Grillet, D. Manchon, E. Cottancin, F. Bertorelle, C. Bonnet, M. Broyer, J. Lermé, and M. Pellarin, J. Phys. Chem. C **117**, 2274 (2013).
[47]M. Ghasemi Varnamkhasti, H. R. Fallah, M. Mostajaboddavati, and A. Hassanzadeh, Vacuum **86**, 1318 (2012).
[48]G. Haacke, J. Appl. Phys. **47**, 4086 (1976).
[49]A. Sangar, A. Merlen, P. Torchio, S. Vedraine, F. Flory, L. Escoubas, L. Patrone, G. Delafosse, V. Chevallier, E. Moyen, and M. Hanbucken, Sol. Energy Mater. Sol. Cells **117**, 657 (2013).
[50]M. Tabatabaei, A. Sangar, N. Kazemi-Zanjani, P. Torchio, A. Merlen, and F. Lagugné-Labarthet, J. Phys. Chem. C **117**, 14778 (2013).
[51]M. Berginc, U. Opara Krasovec, E. Quesnel, and M. Topic, in *2012 38th IEEE Photovoltaics Specalists Conference* (IEEE, 2012), pp. 000015–000020.